# Simulations and experiments of intense ion beam current density compression in space and time[a]

A. B. Sefkow,[1,b] R. C. Davidson,[2] E. P. Gilson,[3] I. D. Kaganovich,[2] A. Anders,[3] J. E. Coleman,[3] M. Leitner,[3] S. M. Lidia,[3] P. K. Roy,[3] P. A. Seidl,[3] W. L. Waldron,[3] S. S. Yu,[3] and D. R. Welch[4]

[1]*Sandia National Laboratories, Albuquerque, New Mexico 87185, USA*
[2]*Princeton Plasma Physics Laboratory, Princeton, New Jersey 08543, USA*
[3]*Lawrence Berkeley National Laboratory, Berkeley, California 94720, USA*
[4]*Voss Scientific, Albuquerque, New Mexico 87108, USA*

The Heavy Ion Fusion Science Virtual National Laboratory has achieved 60-fold longitudinal pulse compression of ion beams on the Neutralized Drift Compression Experiment (NDCX) [P. K. Roy *et al.*, Phys. Rev. Lett. **95**, 234801 (2005)]. To focus a space-charge-dominated charge bunch to sufficiently high intensities for ion-beam-heated warm dense matter and inertial fusion energy studies, simultaneous transverse and longitudinal compression to a coincident focal plane is required. Optimizing the compression under the appropriate constraints can deliver higher intensity per unit length of accelerator to the target, thereby facilitating the creation of more compact and cost-effective ion beam drivers. The experiments utilized a drift region filled with high-density plasma in order to neutralize the space charge and current of an $\sim 300$ keV $K^+$ beam and have separately achieved transverse and longitudinal focusing to a radius $<2$ mm and pulse duration $<5$ ns, respectively. Simulation predictions and recent experiments demonstrate that a strong solenoid ($B_z < 100$ kG) placed near the end of the drift region can transversely focus the beam to the longitudinal focal plane. This paper reports on simulation predictions and experimental progress toward realizing simultaneous transverse and longitudinal charge bunch focusing. The proposed NDCX-II facility would capitalize on the insights gained from NDCX simulations and measurements in order to provide a higher-energy ($>2$ MeV) ion beam user-facility for warm dense matter and inertial fusion energy-relevant target physics experiments. © *2009 American Institute of Physics*. [DOI: 10.1063/1.3078424]

## I. INTRODUCTION

There are many challenges to the development of heavy-ion drivers[1] for applications such as warm dense matter physics,[2] high-energy-density physics,[3] and the heavy ion fusion approach to inertial fusion energy.[4–6] The size and cost of an ion beam driver are strongly dependent on the amount of acceleration and compression (in space and time) that can be achieved. The general description of an ion driver for heavy ion fusion is as follows. Multiple beams are created from short-pulse, high-current ion injectors, which are matched to electric and/or magnetic focusing accelerators responsible for increasing the energy of the beams. Transport and compression sections follow, where both the beam density and total current of each beam must rapidly increase after final focusing trajectories are imparted to the beam ions. The beams longitudinally converge in the target chamber with approximate currents of up to tens of kiloamperes per bunch and pulse durations $<10$ ns. The beams must also be transversely focused to spot sizes no larger than approximately 2 mm in order to achieve the necessary intensities for striking the target.[7,8] In addition to providing high levels of compression required for sufficient and optimal energy density on target, some of the other challenges that need to be evaluated and mitigated include emittance growth, alignment and acceleration errors, longitudinal stability, dispersion, chromatic and geometric aberration, and multibeam interaction instabilities.

The primary challenge for the heavy ion fusion approach to inertial fusion energy has traditionally been to reduce the cost of the accelerator. However, ion drivers can deliver more intensity to the target per unit length of accelerator by greatly compressing the beams simultaneously in space (small transverse spot size) and time (short pulse duration), as shown in Fig. 1. The cost of an ion beam driver dramatically decreases with the amount of total current density compression (transverse plus longitudinal/axial) that can be achieved over a short distance. As the amount of compression that can be realized increases, the ion driver can deliver the same power on target at lower beam energies. The acceleration of ion beams to high energies is the most costly aspect of building an ion driver. Therefore, compression optimization under the appropriate experimental constraints enables the use of more compact and cost-effective accelerators than previously envisioned, allowing ion beam drivers to become more competitive with other technologies.

The outline of this paper is as follows. Section II introduces the technique of plasma-assisted focusing to achieve high levels of intense ion beam compression (beyond the
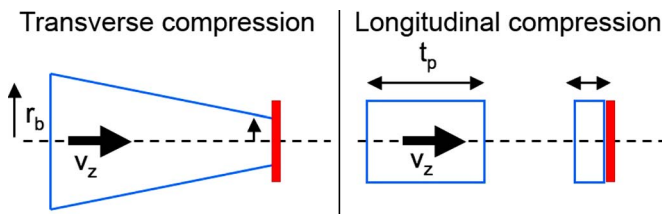
---

FIG. 1. (Color online) Concept depiction of transverse (spatial) and longitudinal/axial (temporal) charge bunch compression. The beam travels along the $z$ axis with velocity $v_z$. Both types of compression are critical for achieving high intensities on target, since power per unit area is $\sim r_b^{-2}$ and $\sim t_p^{-1}$.
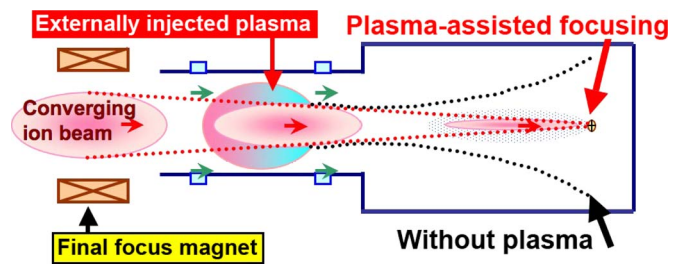


FIG. 2. (Color online) Concept depiction of plasma-assisted transverse focusing. Space charge and current neutralization of the intense charge bunch allows the beam to focus to its emittance-dominated spot size.

traditional space-charge limit), and also discusses the Neutralized Transport Experiment (NTX) and Neutralized Drift Compression Experiment (NDCX) devices. Several of the experimental limitations of longitudinal compression are presented in Sec. III. Section IV reports the simulation predictions and experimental progress of simultaneous transverse and longitudinal compression to a coincident focal plane. Future plans for the upgraded NDCX-II device and a brief summary of results are provided in Sec. V.

## II. PLASMA-ASSISTED ION BEAM FOCUSING

Simultaneous transverse and longitudinal current density compression to small spot sizes and short pulses, respectively, is essential to heavy ion fusion, since the power per unit area is inversely proportional to (a) the square of the beam radius and (b) the pulse duration. Plasma-assisted focusing is critically required for achieving very high levels of transverse and longitudinal compression because of the inherently defocusing nature of the electric self-fields of space-charge-dominated beams. If the beam current is large enough, magnetic self-fields can also become important to control. Plasma-assisted focusing entails the external injection of a dense plasma into the propagation path of the beam after a focusing trajectory has been applied to the intense charge bunch. The self-fields of intense charge bunches can be neutralized by the background plasma, and the beams can propagate stably and quiescently at high intensities,[9,10] provided that the plasma density is sufficiently larger than the beam density.[11] In the case of transverse focusing to a small spot size, the ion beam is given a radially convergent angle by the final-focus magnet at the end of the transport section, which lies between the source and target chamber, as illustrated in Fig. 2. As an example, consider a 4 MJ heavy-ion driver consisting of sixteen 4 GeV Cs$^+$ beams. If each beam carries 6.25 kA of current within a 2 mm radius and pulse duration <10 ns, the total power would be approximately 400 TW. The peak density of each beam is then approximately $4 \times 10^{13}$ cm$^{-3}$, and a plasma whose density is approximately an order-of-magnitude higher would be desired to provide sufficient levels of neutralization for plasma-assisted focusing. The beam then passes through a neutralized drift section filled with plasma, where the space charge of the intense beam can be well neutralized, and the charge bunch can be transversely focused to its emittance-dominated spot at a focal plane specified by the final-focus

magnet. When plasma is not present in the chamber, the beam radially defocuses under its own space-charge forces, resulting in a much larger spot size at the intended focal plane.

The NTX at the Lawrence Berkeley National Laboratory was a scaled experiment for ion drivers, and it studied plasma-assisted transverse focusing of intense ion beams to small spot sizes.[12,13] The K$^+$ ion source could produce 200–400 keV beams with approximately 10–80 mA of current. Also, the injector could create beams with perveances (approximately defined as the ratio of the space-charge potential to the beam energy) up to 10$^{-3}$. The perveance is an important dimensionless quantity used to characterize the suitability of beam systems for un-neutralized or neutralized transport (requiring plasma to neutralize the space-charge forces). Typical initial beam radii and temperatures were approximately 1–2 cm and 0.2 eV, respectively. A magnetic transport section, consisting of solenoids or quadrupoles, transported the beam downstream to another section containing a dense plasma column for neutralization experiments and a diagnostic box. The low pressure (<10$^{-6}$ torr) maintained in the NTX device helps prevent charge-exchange processes and the stripping of beam ions to higher charge states, which can raise the beam emittance and reduce the achievable amount of compression; such scattering and stripping effects of the beam ions can become an issue, which needs to be carefully evaluated and mitigated, in experiments using more energetic ion beams (e.g., a heavy ion driver). As revealed in Fig. 3, the NTX device successfully demonstrated the ability to focus intense space-charge-dominated beams to small spot sizes by utilizing a plasma-filled drift region downstream of the final-focus magnet.[12,14] Physics results obtained on the NTX device are directly applicable to larger ion beam drivers for heavy-ion fusion because of the dimensionless parameter regime available in the experiments.[13]

The upgrade to the NTX device is the NDCX, and its goal is to study longitudinal (temporal) plasma-assisted focusing.[15,16] The primary component addition to the NDCX device is a linear induction accelerator, also known as the induction bunching module. The induction module is located between the final transport magnet and the neutralized drift region containing the dense plasma. Particle-in-cell (PIC) simulations[17] using the code LSP[18] are employed to self-consistently model the beam and plasma dynamics from the final transport magnet to the target plane in the diagnostic box. The induction module utilizes Faraday's law to impart
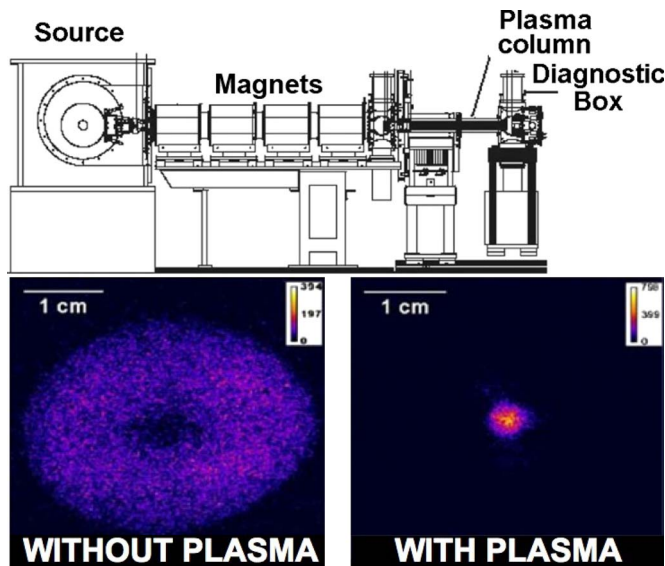
FIG. 3. (Color online) NTX schematic (top) and transverse scintillator images (bottom) comparing experiments without plasma-assisted focusing (bottom left) and with plasma-assisted focusing (bottom right).



FIG. 5. (Color online) The ideal voltage waveform $V_{app}(t)$ for $E_0$ =400 keV, $f$=0.5, and $t_p$=300 ns (top) and the resulting longitudinal compression ratio $I_b(t)/I_b^0$ at multiple axial locations near the focal plane, in steps of $\Delta z$=0.1 cm (bottom). Numerically "infinite" compression with vanishing $t_{FWHM}$ is recovered for the cold ($T_b$=0) beam case, assuming complete neutralization of the beam by the plasma.

an induced emf axial electric field, $E_z(t)$, along the path of a passing ion beam, across a small opening in the induction accelerator known as an acceleration gap. The principal features of longitudinal ion beam compression using a linear induction accelerator are represented in Fig. 4. Essentially, an applied time-dependent voltage pulse and its associated current result in an amplified azimuthal magnetic field in the ferromagnetic core of the induction module, which encircles the beam pipe. Since the current and magnetic fields are time dependent, the induced axial electric fields are also time dependent. The electric field acts on the passing ion beam across the acceleration gap, and the voltage pulse and its polarity are timed such that the head/tail of the beam is subject to a decelerating/accelerating axial electric force. Therefore, the beam acquires a head-to-tail axial velocity tilt (or "ramp"), $v_z(t)$, which is responsible for longitudinally compressing the beam throughout the plasma drift region to high current and short pulse duration at the focal plane;[19] longitudinal focusing research of a similar nature has been conducted by the light ion fusion and magnetically insulated diode communities,[20,21] except the common terminology

used therein is longitudinal "bunching" and "point of bunching" rather than "focusing" and "focal plane."

## III. LIMITATIONS OF LONGITUDINAL COMPRESSION

There exists an ideal voltage waveform for the induction module that results in ideal longitudinal compression; assuming complete neutralization of the beam by the plasma, an ideally induced $E_z(t)$ across an infinitely thin acceleration gap can cause all particles within a perfectly cold (zero temperature, $T_b$=0) beam to arrive at a longitudinal focal plane at the exact same time.[22] The applied voltage waveform $V_{app}(t)$ is specific to one particular (and constant) beam energy $E_0$ entering the acceleration gap and can be specified by two parameters, as depicted in Fig. 5. The first is the fractional velocity tilt $f$, defined as the total axial velocity spread $\Delta v_z/v_z^0$ to be imparted to the beam; $f$ is proportional to the voltage swing (positive to negative) available to the induction module. The second is the intended initial pulse duration $t_p$ to undergo longitudinal compression, which is also the amount of time required for $V_{app}(t)$ to modify the axial velocity phase space of the beam. The desired values of $f$ and $t_p$ are adjustable in the experiments, but are limited in practice by voltage hold-off in the gap, the drift length $L_d$ to the focal plane (set by the plasma section and diagnostic box), and the available volt-seconds or flux of the induction module.

The figures of merit at the focal plane for longitudinal focusing are the current compression ratio, defined as the ratio of peak beam current to the initial beam current ($I_b^{max}/I_b^0$), and the full width at half maximum pulse duration $t_{FWHM}$. Current rather than current density is quoted to characterize longitudinal compression because the diagnostic in use collects the entire beam and so measures the absolute current of the beam in the presence of plasma. As discussed above, the achievement of ideal longitudinal compression in
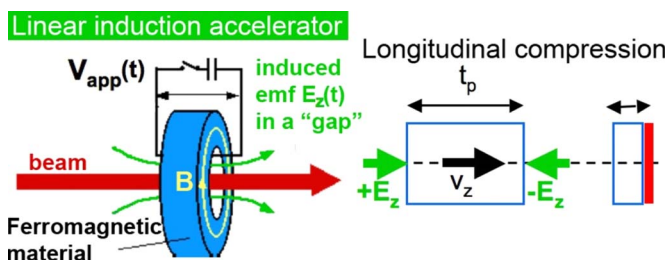


FIG. 4. (Color online) Concept depiction of longitudinal compression using a linear induction accelerator. An applied voltage $V_{app}(t)$ can induce an axial emf $E_z(t)$ across an acceleration gap such that a head-to-tail axial velocity tilt $v_z(t)$ is imparted to the passing ion beam.
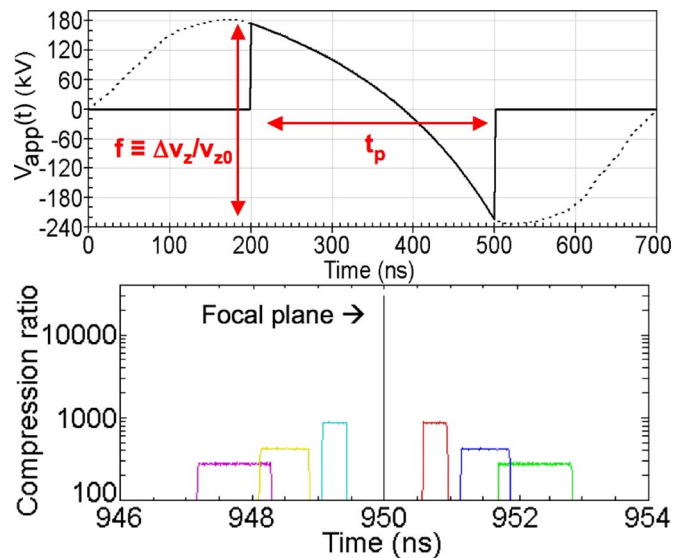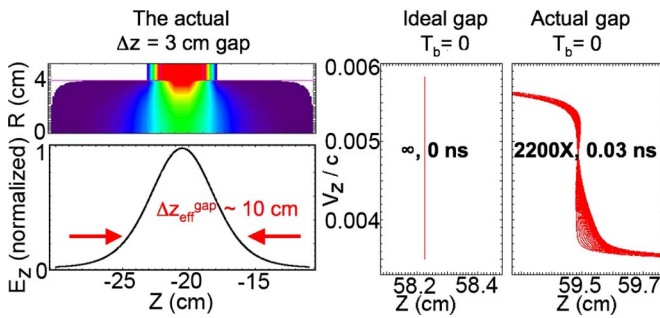
FIG. 6. (Color online) The actual NDCX gap (top left) has a width of $\Delta z = 3$ cm at $r_w = 3.8$ cm, but an effective on-axis ($r = 0$) width $\Delta z_{\rm eff}^{\rm gap} \sim 10$ cm (bottom left) due to boundary conditions. Ion transit-time effects across the $\Delta z_{\rm eff}^{\rm gap}$ introduce a spread (focusing aberration) in the beam's $\{z, v_z/c\}$ phase space (right), resulting in a reduced $I_b^{\rm max}/I_b^0$ and an increased $t_{\rm FWHM}$ relative to the infinitely thin ideal-gap case. $[I_b^{\rm max}/I_b^0, t_{\rm FWHM}]$ values are overlaid on the phase space plots.
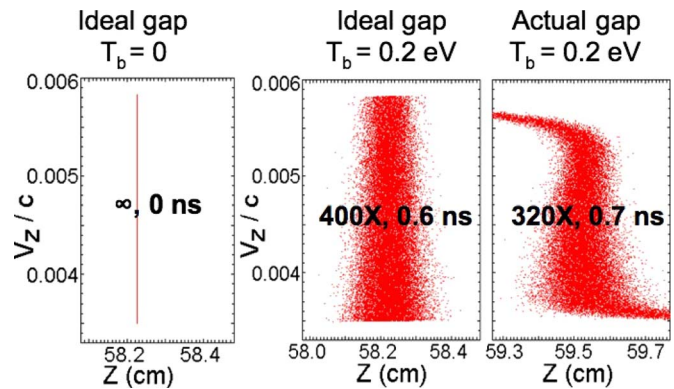


FIG. 7. (Color online) Beam $\{z, v_z/c\}$ phase space at the longitudinal focal plane for $T_b = 0$ and the ideal gap (left), $T_b = 0.2$ eV and the ideal gap (middle), and $T_b = 0.2$ eV and the actual gap (right). $[I_b^{\rm max}/I_b^0, t_{\rm FWHM}]$ values are overlaid.

the classical limit would result in infinite current compression and vanishingly small $t_{\rm FWHM}$. An example of ideal longitudinal compression for $E_0 = 400$ keV, $f = 0.5$, and $t_p = 300$ ns is also provided in Fig. 5. The numerical maximum compression ratio of 30 000 and $t_{\rm FWHM} = 0.01$ ns for $t_p = 300$ ns and a time step of $\Delta t = 0.01$ ns are recovered at the focal plane $L_d = 78.7$ cm in PIC simulation involving complete neutralization of the beam by the plasma.[22] Although no classical bound exists for ideal longitudinal compression, such ideal circumstances are not achievable in the laboratory.

The nonzero length of the acceleration gap itself sets a finite upper bound on realizable longitudinal compression ratios. In the NDCX device, the gap is $\Delta z = 3$ cm at a wall radius $r_w = 3.8$ cm, but the boundary conditions result in an effective $E_z$ axial extent on axis (at $r = 0$) of $\Delta z_{\rm eff}^{\rm gap} \sim 10$ cm, as is evident in Fig. 6. The transit time of an $E_0 = 400$ keV $K^+$ ion across such an effective length is $\sim 75$ ns, which is a significant fraction of the pulse time for $V_{\rm app}(t)$ (i.e., $t_p$). The temporal and spatial dependences of the radial and axial electric fields in the finite-size gap result in transverse and longitudinal phase space coupling, such that particles entering the gap at different radii receive differing amounts of integrated axial electric forces because of (a) significant radial motion and (b) changes in $V_{\rm app}(t)$ from one end of the gap to the other. As a result, the $\{z, v_z\}$ phase space of the exiting beam contains more spread relative to an ideal-gap case, as displayed in Fig. 6; this effective longitudinal beam temperature increase (from $T_b = 0$) causes compression ratio degradation and increased amounts of aberration (increased $t_{\rm FWHM}$) at the focal plane.[22] In this paper, nonideal interactions between beam particles and the voltage $V_{\rm app}(t)$ applied across the finite size of the gap are referred to as the "gap effects."

Experimentally realizable intense ion beams have some *nonzero* initial longitudinal temperature $T_b$, which further reduces the upper limits of achievable longitudinal compression. Therefore, there are effectively two sources of longitudinal focusing aberration: the inherent initial $T_b$ and the effective $T_b$ increase imparted to the beam by the gap and the applied voltage $V_{\rm app}(t)$. For representative NDCX parameters, the transit-time effects increase the effective $T_b$ by ap-

proximately 45%, which correspondingly reduces the compression by about 20%. PIC simulations using an ideal gap show that the compression ratio decreases to $I_b^{\rm max}/I_b^0 = 400$ and the pulse duration increases to $t_{\rm FWHM} = 0.6$ ns when the realistic value $T_b = 0.2$ eV of the NDCX beam is included (compared to $\infty$ and 0 ns for $T_b = 0$). When the gap size and $V_{\rm app}(t)$ are also taken into account, the values further decrease to $I_b^{\rm max}/I_b^0 = 320$ and increase to $t_{\rm FWHM} = 0.7$ ns, respectively, as portrayed in Fig. 7. Analytic theory and PIC simulations show that longitudinal compression ratios decrease and pulse durations increase proportionally to the square of the longitudinal $T_b$ ($I_b^{\rm max}/I_b^0 \sim T_b^{-0.5}$, $t_{\rm FWHM} \sim T_b^{+0.5}$).[22,23]

Consider variations in the voltage waveform $V_{\rm app}(t)$ parameter $t_p$, the initial temporal pulse duration of the beam intended to undergo longitudinal compression. Figure 8 offers five waveforms and the resulting temporal compression
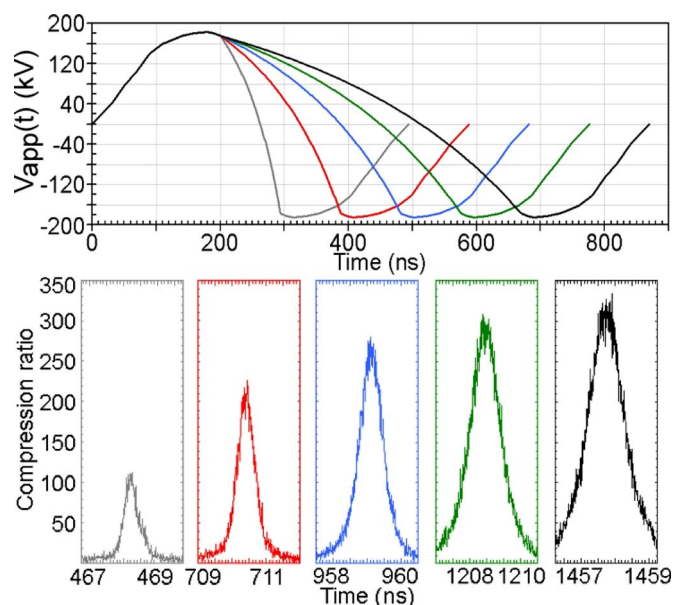


FIG. 8. (Color online) Voltage waveforms $V_{\rm app}(t)$ for $E_0 = 400$ keV and $f = 0.5$, with $t_p$ varying from 100 to 500 ns (top), and the resulting color-coded longitudinal compression ratios $I_b(t)/I_b^0$ (including gap effects and $T_b = 0.2$ eV) at the focal planes.
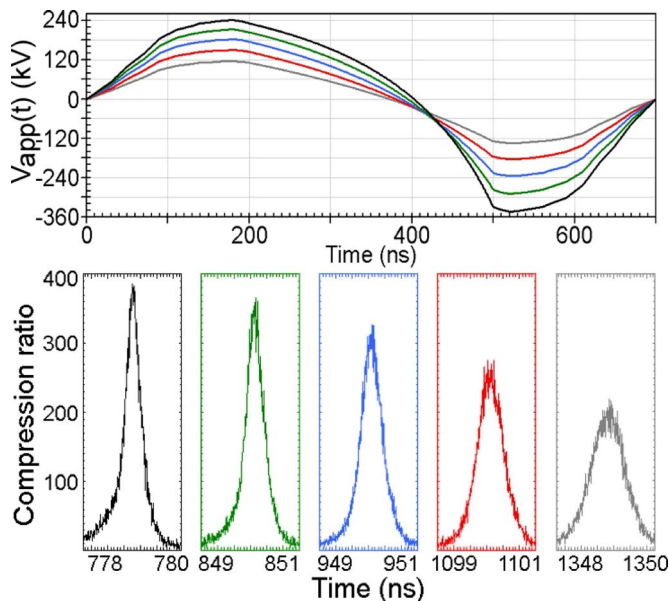
FIG. 9. (Color online) Voltage waveforms $V_{app}(t)$ for $E_0=400$ keV and $t_p =300$ ns, with $f$ varying from 0.3 to 0.7 (top), and the resulting color-coded longitudinal compression ratios $I_b(t)/I_b^0$ (including gap effects and $T_b =0.2$ eV) at the focal planes.



FIG. 10. (Color online) Comparison between an experimentally realized $V_{app}(t)$ and ideal $V_{app}(t)$ (left) and between longitudinal compression measurement, PIC simulation, reduced kinetic model, and reduced hybrid fluid-Vlasov model (right).

for $t_p$ varying from 100 to 500 ns in steps of 100 ns, with fixed $f=0.5$, $T_b=0.2$ eV, and $E_0=400$ keV. For $t_p \geq 300$ ns, the compression ratios increase as $I_b^{max}/I_b^0 \sim t_p^{+0.3}$, but the pulse durations increase as $t_{FWHM} \sim t_p^{+1}$. Since $t_{FWHM}$ increases more rapidly than the compression ratios for all but the shortest $t_p$ cases, an effect of diminishing returns is evident.[22] Longer $t_p$ values yield more current compression at the cost of more rapidly increasing amounts of aberration associated with the longer drift lengths $L_d$.

Similarly, consider variations in the voltage waveform $V_{app}(t)$ parameter $f$, the intended fractional axial velocity tilt. Figure 9 presents five waveforms and the resulting temporal compression for $f$ values varying from 0.3 to 0.7 (or 30% to 70%) in steps of 0.1, with fixed $t_p=300$ ns, $T_b=0.2$ eV, and $E_0=400$ keV. For $f \leq 0.5$, the compression ratios increase as $I_b^{max}/I_b^0 \sim f^{+0.82}$, whereas they increase as $f^{+0.51}$ for $f \geq 0.5$. The pulse durations decrease with $f$ as $t_{FWHM} \sim f^{-1.23}$ (for all $f$), in agreement with analytic theory ($t_{FWHM} \sim f^{-1.25}$).[22] In general, larger $f$ values are more desirable because they yield higher compression in experiments; however, the achievable values of $f$ in the laboratory are limited by the available $L_d$, voltage hold-off in the gap, and available volt-seconds or flux of the induction module. In addition, larger values of $f$ can lead to increased amounts of transverse focusing aberration in simultaneous transverse and longitudinal focusing experiments.

The predictions from reduced theoretical models (a kinetic model using self-similar drift compression solutions without gap effects[24,25] and a hybrid fluid-Vlasov model[25]) and PIC simulations are in excellent agreement with NDCX measurements.[25] Figure 10 plots a comparison between an experimentally realized waveform $V_{app}(t)$ and an ideal waveform. The hybrid fluid-Vlasov model, a kinetic formalism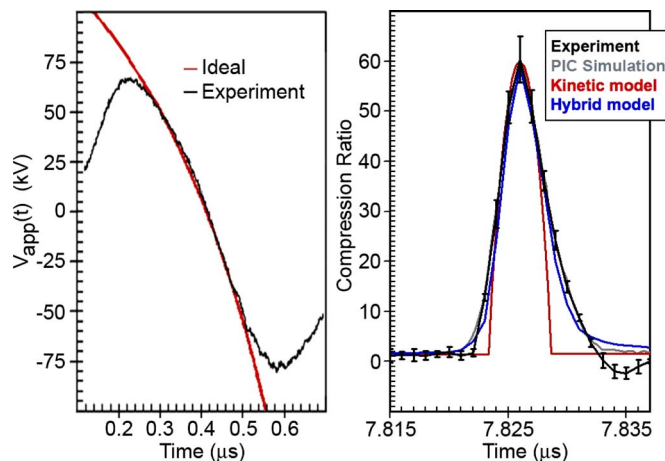 based on the Vlasov equation that has been initialized with parameters from a collisionless warm-fluid model, and PIC simulations include the finite-size gap and experimental $V_{app}(t)$, whereas the kinetic model does not include either (rather, it assumes a linear velocity tilt is imposed on the beam at time $t=0$). The experimental $V_{app}(t)$ achieves an approximate value of $f \sim 0.15$ and contains some inaccuracy near the maximum and minimum voltages, as well as some intermediate deviations; simulations estimate that the discrepancy between the ideal and experimental voltages results in longitudinal compression degradation by approximately a factor of 2–3. A "pinhole" fast Faraday cup was specifically designed to measure the absolute beam current $I_b(t)$ in the presence of the neutralizing plasma,[26] and its signal is given in Fig. 10 for the NDCX beam parameters $E_0 \sim 320$ keV, $I_b^0 \sim 20$ mA, $r_b^0 \sim 2$ cm, and $T_b \sim 0.2$ eV. The hybrid fluid-Vlasov model and PIC simulation reproduce the experimentally measured compression ratio within 5%, as shown in Fig. 10 (the error bars represent the 95% confidence interval in the mean of four shots). A compression ratio of $I_b^{max}/I_b^0 \sim 60$ and pulse duration of $t_{FWHM} \sim 4.5$ ns are predicted by a hybrid fluid-Vlasov model and PIC simulation, but the kinetic model underestimates the pulse duration because it does not include the gap effects that cause additional prepulse and postpulse current formation (the "pedestal") around the central peak in longitudinally compressed current.[25]

## IV. SIMULTANEOUS TRANSVERSE AND LONGITUDINAL FOCUSING

The NDCX longitudinal focusing experiments are very encouraging, and the experimental constraints of temporal compression are well understood because of detailed modeling efforts and comparison to measurements. However, optimized simultaneous transverse and longitudinal compression to a coincident focal plane[27] is desired for target experiments. Although the initial NDCX measurements succeeded in temporally compressing a beam to $I_b^{max}/I_b^0 \sim 60$ and $t_{FWHM} \sim 4.5$ ns, the beam radius ($e^{-1}$) at the focal plane is
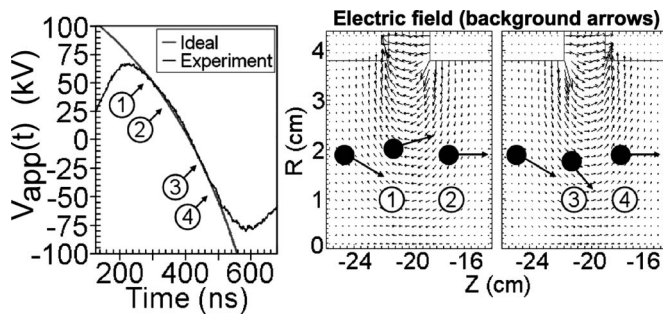
FIG. 11. Illustration of the transverse defocusing effect of the gap during the $dV_{app}(t)/dt < 0$ portion of the voltage waveform for longitudinal compression.

measured to be $r_b^{foc} > 1$ cm even though a converging transverse (radial) focusing angle is applied to the beam using the final magnet in the transport section (just prior to the entering the gap).

## A. The transverse defocusing effect and overfocusing technique

Imposing an axially compressing velocity tilt $v_z(t)$ onto the ion beam across an acceleration gap of finite size results in a deleterious time-dependent transverse (radial) defocusing effect, as elucidated in Fig. 11.[22,23] The longitudinally compressing part of the $V_{app}(t)$ waveform satisfies $dV_{app}(t)/dt < 0$. Due to this fact, and the transit time of the ions across the gap, the radial electric fields $E_r$ (present in the gap because of boundary conditions) affecting the ions on the upstream and downstream ends of the gap do not balance each other. Instead, when $V_{app}(t) > 0$ [$V_{app}(t) < 0$], the ions encounter excess $+E_r$ ($-E_r$) earlier (later) in time on the upstream (downstream) end of the gap compared to the downstream (upstream) end. In other words, beam particles within the compressing $v_z(t)$ velocity tilt receive a net time-dependent divergence due to a positive integrated radial electric force [$\int E_r(t)dt > 0$] across the gap. The transverse defocusing effect is more pronounced for larger $f$ with fixed $t_p$ because $dV_{app}(t)/dt$ is more negative.

The transverse defocusing effect is predicted in PIC simulations. Phase space plots of a transversely focusing NDCX ion beam, with and without an applied $v_z(t)$ tilt, are provided in Fig. 12.[22] Without an applied tilt, the beam focuses to a small spot size in the presence of plasma (not shown). However, when the tilt is applied across the gap (near $z \sim -20$ cm), the beam's $\{z, v_r\}$ phase space is time-dependently altered and excess divergence is imparted to an otherwise radially converging beam. When the radius $r_b^{foc}(t)$ of the beam at the focal plane is considered, the time of best longitudinal focus is found to coincide with the time of *worst* transverse focus. Experiments on the NDCX device corroborate the existence of the defocusing effect,[15,16] as also shown in Fig. 12. Unfortunately, large spot sizes are unsuitable for target heating experiments because the power per unit area (W cm$^{-2}$) depends on the inverse beam radius squared ($r_b^{-2}$).

The simplest method envisioned to offset the transverse defocusing effect in experiments attempting simultaneous transverse and longitudinal focusing is to "overfocus" the

beam with the final-focus magnet in the transport section. For NDCX parameters, when the radially convergent angle $\theta_r$ (quoted in radians as the ratio of the beam radius to the transverse focal length) of the beam into the gap is approximately doubled, the excess applied transverse focusing is balanced by the defocusing effect in a time-averaged sense, and the beam is able to focus to a small spot size coincident with the longitudinal focal plane,[28] as indicated in Fig. 13. The difference between nominal focusing and overfocusing is dramatic: because of the order-of-magnitude difference in $r_b^{foc}$ at the time of peak longitudinal compression, a factor of approximately 100 is recovered in beam number density, as well as in the percentage of energy deposition residing within the compressed pulse. Measurements in the NDCX
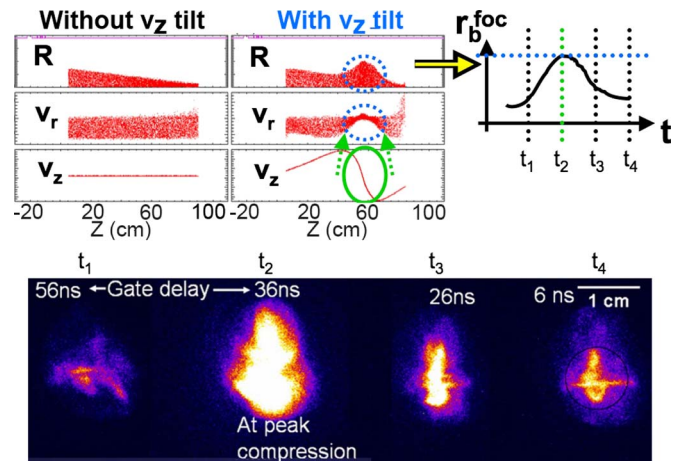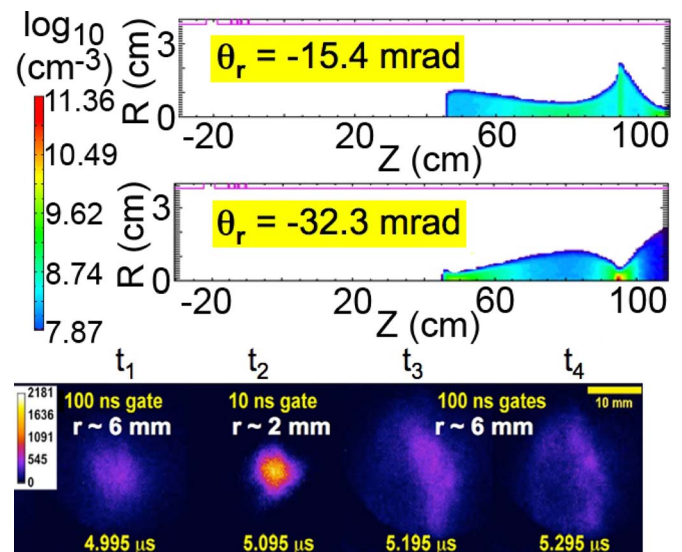


FIG. 12. (Color online) Beam phase space comparison (top) between transverse focusing without (left) and with (middle) a $v_z(t)$ tilt. Excess divergence is imparted to the beam (right), such that the time of best longitudinal focus coincides with the worst transverse focus. Scintillator images corroborated this effect in NDCX experiments (bottom).



FIG. 13. (Color online) Comparison of $\{r, z\}$ beam density plots (log$_{10}$ scale) near the intended simultaneous focal plane between the nominal ($\theta_r = -15.4$ mrad) and overfocusing ($\theta_r = -32.3$ mrad) cases (top) and scintillator images from overfocusing experiments on the NDCX device (bottom).
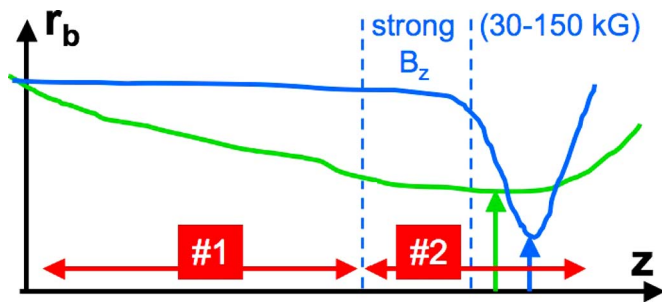
FIG. 14. (Color online) Concept depiction of simultaneous focusing using a strong final-focus solenoid near the focal plane compared to the overfocusing technique. The former case typically achieves smaller spot sizes but requires two plasma sources for beam neutralization.
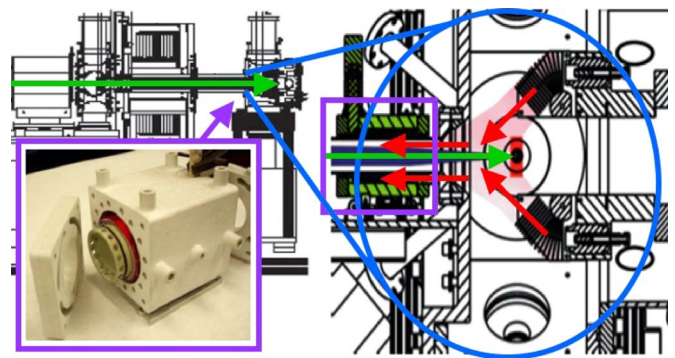


FIG. 15. (Color online) NDCX schematic of plasma injection into a high-field solenoid using two FCAPs. PIC simulations of the downstream region (circled) evaluate whether plasma can be injected into the solenoid (square) and the path of the beam.

device corroborated the suitability of the overfocusing technique for mitigating the defocusing effect,[29] as demonstrated in Fig. 13.

## B. Simultaneous focusing with a strong solenoid

Externally applied magnetic fields are commonly employed to confine, guide, and transversely focus intense ion beams.[19,30,31] If a *final-focus solenoid* is placed near the end of the drift region, smaller beam radii can be achieved at the simultaneous focal plane[22,27] compared to the overfocused case. Figure 14 illustrates a comparison of a typical $r_b(z)$ profile between the two methods for simultaneous focusing. A final-focus solenoid creates a region of strong axial magnetic field $B_z$, and an ion beam will radially focus to a small spot size due to the Lorentz force $-F_r = +q[-v_\theta \times +B_z]$. An ion beam naturally rotates, but it acquires the majority of its rotation for such radial focusing when it encounters the fringe radial magnetic field $-B_r$ at the upstream entrance of the strong solenoid (according to $-F_\theta = +q[+v_z \times -B_r]$).

In most simulated overfocused designs, the minimum beam radius ($e^{-1}$) at the focal plane is $r_b^{foc} \sim 2-3$ mm, and the transverse focal length is approximately as long as the longitudinal focal length. However, in most simulated designs using a final-focus solenoid of strength $B_z \sim 30-150$ kG (situated near the intended focal plane), the minimum beam radius ($e^{-1}$) that can be achieved is approximately $r_b^{foc} \sim 0.25-0.5$ mm (a factor of 16–144 times better than overfocusing considering the $r_b^{-2}$ dependence on power per unit area). In addition, two plasma sources (instead of one) are required to neutralize the beam space charge in a simultaneous focusing design using such a final-focus solenoid because a critically required neutralizing plasma must be present both (a) throughout the main drift length and (b) within the high-field region of the solenoid. Since the transverse focal length is shorter in the strong solenoid case, lower plasma density may be utilized throughout the main drift length, since the beam radius (density) can remain larger (smaller) until the strong solenoid is encountered. However, the need for a critically required neutralizing plasma to be present within the strong solenoid may be problematic for such space-charge-dominated ion beam compression experiments.

The injection of high-density plasma into the high-field region of a final-focus solenoid may be stymied by a well-known plasma physics effect called magnetic mirroring.[32] The magnetic moment of a charge particle, $\mu = mv_\perp^2/2B$, is an adiabatic invariant in the limit of weak collisions. The conservation of $\mu$ and kinetic energy implies that the velocity component of a charged particle parallel to the magnetic field will increase or decrease if the field strength decreases or increases, respectively, along the field line on which the particle moves. The force arising in the direction opposite to the field gradient, $F_\parallel = -\mu \nabla B$, can cause injected plasma moving toward the high-field region of the final-focus solenoid to decelerate and be reflected (i.e., *mirror*) away from the high-field region. Generally, plasma penetration into the high-field region only occurs for magnetized particles whose ratio of parallel to perpendicular velocity (relative to the magnetic field) satisfies $v_\parallel/v_\perp > \sqrt{B_{max}/B_{min} - 1}$, and thereby enter the "loss cone" in velocity space that allows them to penetrate the high-field region.[33]

An important question related to the compression goals of the NDCX device is whether the filtered cathodic-arc plasma source (FCAPS), normally used as the neutralizing background plasma in plasma-assisted focusing experiments, can be employed to inject plasma into the high-field region of a strong solenoid.[27,34] Further PIC simulations have evaluated whether plasma can be injected into the solenoid and the path of the beam,[28] as specified in Fig. 15. The simulations model only the downstream end of the device, where two off-axis FCAPSs inject plasma toward the $r=0$ axis and upstream into the high-field region of the final-focus solenoid.

The plasma injection simulations are carried out in three dimensions (3D) because of the lack of symmetry in the system, as well as the need to evaluate particle motion and drifts in the complex 3D magnetic field topology created by the two off-axis plasma filter coils ($B \sim 0.45$ kG) and the final-focus solenoid ($B \sim 50$ kG). The parameters for the injected Al$^+$ plasma shown in Table I are ion current density, ion temperature, electron temperature, ion velocity (as measured), and ion Mach number, defined as the ratio of ion velocity to sound speed (determined by $\sqrt{[T_e + \gamma T_i]/m_i}$). In this coordinate system, the beam travels in the $-\hat{y}$ direction,

TABLE I. Simulated FCAPS injection parameters.

| $J_i$ | $T_i$ | $T_e$ | $v_i$ (expt.) | $M_i \equiv v_i/C_s$ |
|---|---|---|---|---|
| 2  A cm$^{-2}$ | 3 eV | 10 eV | 1.44  cm $\mu$s$^{-1}$ | 1.7 |

and the two FCAPSs are located off the $z$ axis and inject plasma in the $+\hat{y}$ direction.

Simulated steady-state plasma density profiles in $\{y,z\}$ space and experimental intensified charge-coupled device (ICCD) camera images of plasma flow under approximately similar conditions are shown in Fig. 16. Simulations predict[27,28] and experiments confirm[34,35] that the crucial beam-neutralizing plasma enters the strong field region of the final-focus solenoid. The ICCD camera employs a narrow-band filter to selectively record the emission from excited N$_2^+$ at 391 nm. In the figure, both weak and strong magnetic field cases are shown. The qualitative comparison between the predictions from simulations and experimental camera images is very good; quantitative plasma density comparisons are in progress. The cathodic-arc plasma sources create supersonic plasma ($M_i > 1$) and thereby have a higher proportion of plasma particles satisfying the necessary $v_\parallel/v_\perp$ condition required to enter the velocity space loss



FIG. 17. (Color online) Plasma density (log$_{10}$ scale) of main drift length plasma (top left) and FCAPS injection (top right) into a final-focus solenoid (marked "Sol.") with length $\sim$10 cm and strength $B_z \sim 50$ kG. The simulation predicts a spot size of $r_b^{foc} \sim 2$  mm (bottom left) and agrees well with the transverse scintillator image of the simultaneously focused beam at time of peak longitudinal compression (bottom right).

cone and penetrate into the high-field region. Therefore, the amount of plasma density able to penetrate the high-field region is sensitively dependent on the injection velocity of the plasma ions. Simulations predict[28] and experiments confirm[35] that plasmas with larger ion Mach numbers are able to penetrate the high-field region of the solenoid with larger peak plasma densities.

As the inset of the transverse $\{x,y\}$ plasma profile in the strong field simulation of Fig. 16 shows, the shape and amount of radial plasma fill, as well as the amount of azimuthal symmetry, are areas of concern. Simulations predict that simultaneous beam compression will generally not be optimal if the beam entering the final-focus solenoid has a larger radius than that of the plasma existing within the high-field region due to lack of adequate neutralization. Similarly, if the plasma density peaks off the $r=0$ axis, where the beam density and space charge are maximum for a centered beam, charge neutralization may also be incomplete. Likewise, azimuthal asymmetry in the plasma profiles may also impact neutralization of the beam. By increasing the separation distance between the FCAPS and the final-focus solenoid, simulations predict that the azimuthal asymmetry can be mitigated because of the extra time/distance the plasma has to execute 3D drifts in the transverse directions.

Experiments showing simultaneous charge bunch focusing in space and time are underway in the NDCX device using two plasma sources. Realistically injected plasma profiles from the main drift length plasma and the FCAPS injection of plasma into a final-focus solenoid are furnished in Fig. 17. The solenoid is approximately 10 cm long with a peak magnetic field of $B_z \sim 50$ kG, and its location is also provided in the figure. An integrated beam-plasma PIC simulation of this experiment predicts a radius ($e^{-1}$) of approximately 2 mm at the longitudinal focal plane, in agreement with the measurements.[23,34] The experimenters measure the longitudinal compression $I_b(t)/I_b^0$ of the beam, and then a time-gated scintillator plate is used to record the transverse profile at the time of peak temporal compression.
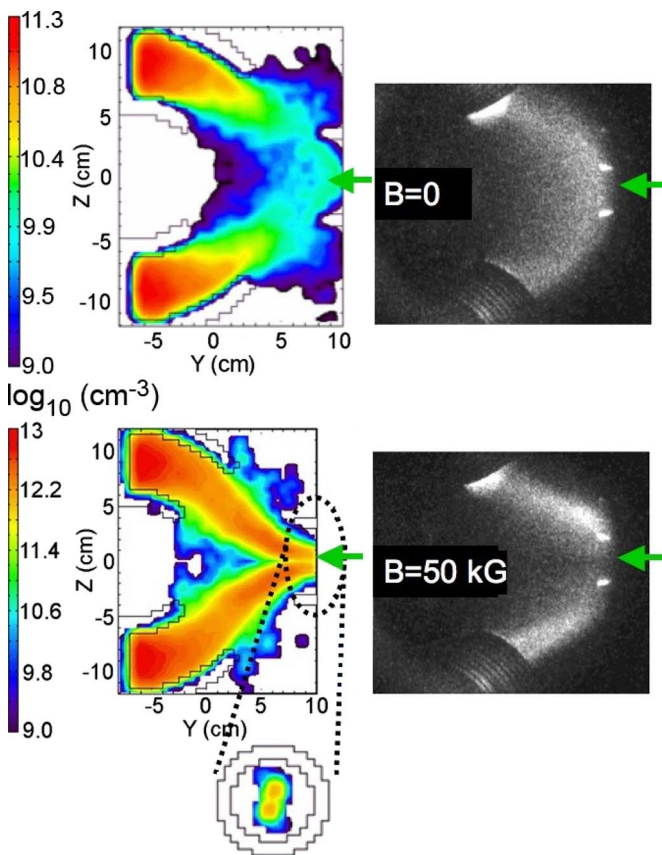


FIG. 16. (Color online) Comparison of simulated plasma density profiles (left) and experimental camera images (right) of injection into a weak (top) and strong (bottom) final-focus solenoid. The inset of the strong field simulation shows asymmetrical plasma fill in the transverse $\{x,y\}$ plane within the solenoid. The location of the beam axis and direction of beam propagation are illustrated by arrows.
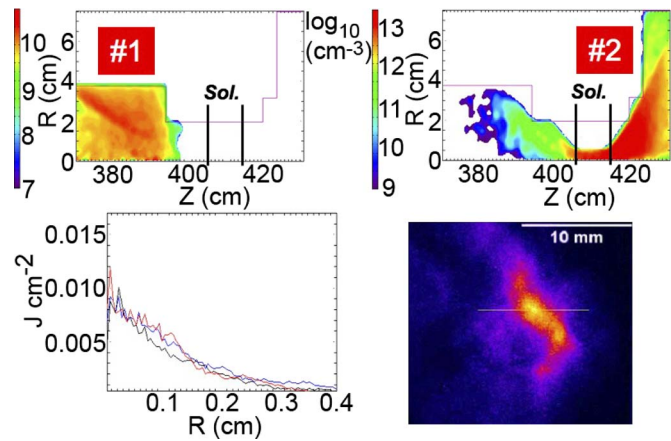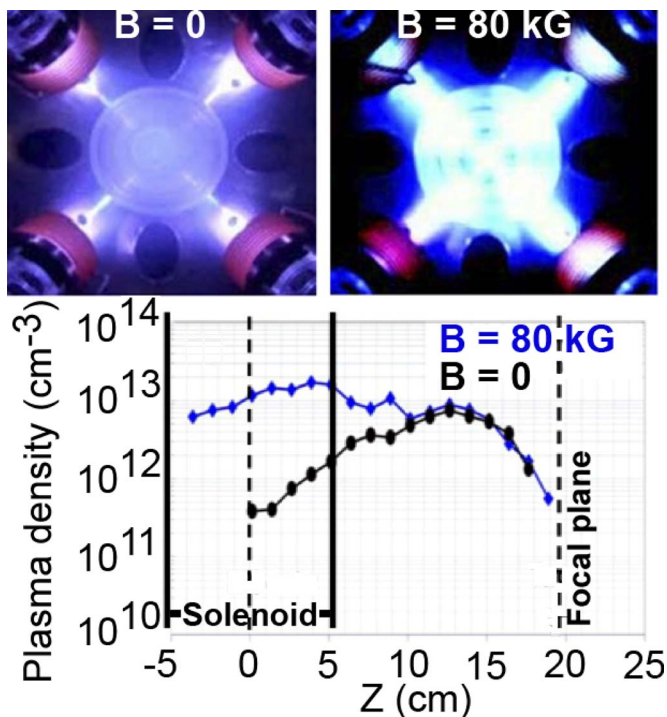
FIG. 18. (Color online) Digital camera pictures of an arrangement of four FCAPSs in operation without (top left) and with (top right) a powered final-focus solenoid. The magnetic fringe fields of the solenoid act as guide channels for the plasma flow, and the strong field compresses the plasma density.
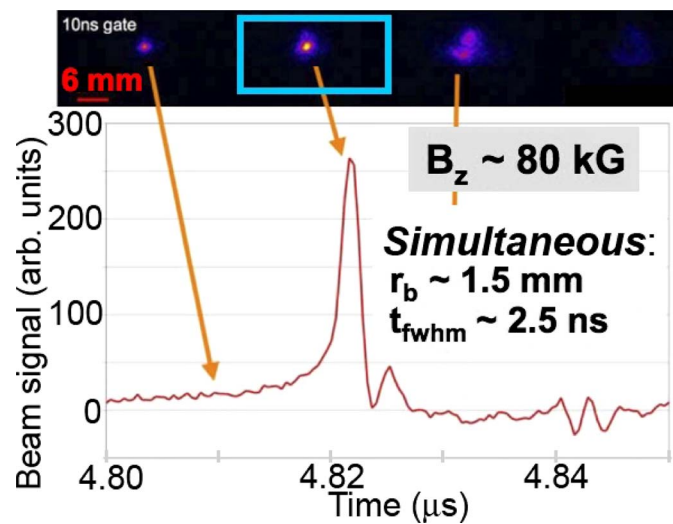


FIG. 19. (Color online) Time-gated transverse beam profile scintillator images (top) and temporal measurement of beam current (bottom) at the simultaneous focal plane. In this simultaneous focusing experiment, the use of a final-focus solenoid results in a coincident spot size $r_b^{foc} \sim 1.5$ mm (50% enclosed flux) and pulse duration $t_{FWHM} \sim 2.5$ ns.

In order to assess the plasma density profiles upstream of, within, and downstream of the final-focus solenoid, a diagnostic consisting of 37 Langmuir probes arranged in a hexagonal pattern (for $\{r, \theta\}$ resolution) and mounted to move along the beam axis (for $z$ resolution) has been fabricated.[35] Preliminary experiments demonstrate that an arrangement of four FCAPSs (instead of two) with straight filter coils (instead of bent coils) greatly increases the achievable plasma densities. As shown in Fig. 18, the magnetic fringe fields of the final-focus solenoid act as guide channels for the plasma flow into the high-field region. Since a stronger $B_z$ field transversely focuses the beam to a smaller spot size, the final-focus solenoid is operated at its approximate peak value of $B_z \sim 80$ kG. The strong field also adiabatically compresses to high density the plasma that is able to penetrate into the solenoid. Furthermore, experiments are determining whether the plasma fill within the solenoid is peaked on the $r = 0$ axis and whether azimuthal uniformity is present. Initial results are encouraging and show high-density plasma penetrating to a radius of $r_p \sim 3-5$ mm,[35] in approximate agreement with simulation predictions ($r_p \sim 5-6$ mm).[27,28] Experiments are underway to determine the degree of azimuthal symmetry, as well as optimize the arrangement of the system components in order to maximize the plasma density and radial fill within the solenoid.

The best results to date of simultaneous transverse and longitudinal focusing experiments on the NDCX device using a final-focus solenoid (operating at $B_z \sim 80$ kG) are presented in Fig. 19.

## V. FUTURE WORK AND SUMMARY

Work is underway to specify the accelerator architecture and beam physics of the planned upgrade to the NDCX device, called NDCX-II, which will study warm dense matter heated by intense ion beams, as well as the physics of ion direct drive for inertial fusion energy applications.[36,37] The presently envisioned architecture of NDCX-II is displayed in Fig. 20. The simultaneous transverse and longitudinal charge bunch focusing methods for NDCX-II are planned to be similar to the NDCX device. A high-current, short-pulse injector will be used to create either a Li$^{+1}$ or a Na$^{+3}$ ion beam, which will be matched with solenoids into the accelerator. Approximately 30 induction acceleration cells from the decommissioned Advanced Test Accelerator facility at Lawrence Livermore National Laboratory will be refurbished and used to accelerate and longitudinally compress the beam to 3–16 MeV and $t_{FHWM} \sim 1$ ns, respectively, over a distance of about 14 m. Solenoidal focusing elements will
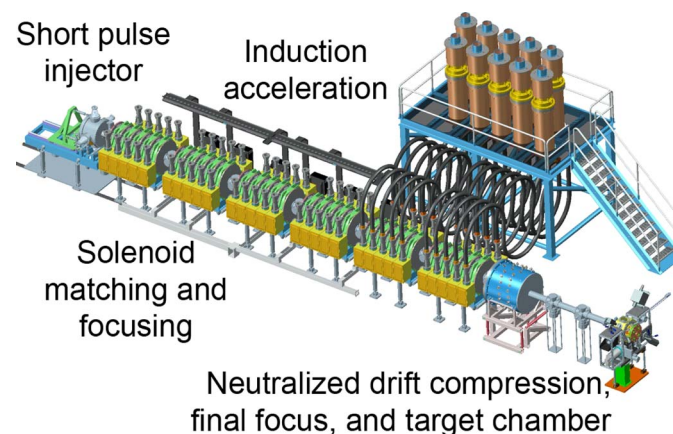


FIG. 20. (Color online) Accelerator architecture schematic of the proposed upgrade to NDCX, called NDCX-II.

TABLE II. Comparison of approximate best values.

| Parameter | NDCX (to date) | NDCX-II (anticipated) |
|---|---|---|
| Ion | $K^{+1}$ | $Li^{+1}$ or $Na^{+3}$ |
| $E_b^{max}$ | 400 keV | 3–16 MeV |
| $r_b^{foc}$ (mm) | 1.5–3 | 0.5 |
| $t_{FWHM}$ (ns) | 2–4 | 1 |
| $I_b^{max}/I_b^0$ | 60 | 500 |
| $I_b^{max}$ (A) | $\sim 2$ | $\sim 30$ |
| $P_{target}$ | 5–20 kbar | 0.25–1 Mbar |

be used in tandem to provide transverse confinement. As in NTX and NDCX, a neutralized drift region will provide plasma-assisted final focusing upstream of the target chamber. A comparison is provided in Table II of the approximate best values of several important parameters measured on the NDCX and those anticipated (simulated) for the NDCX-II. The parameters in Table II are ion species, maximum beam energy, minimum radius at focus, pulse duration at focus, longitudinal compression ratio, peak current, and energy density (pressure) delivered to a target located at the focal plane.

In summary, simulation predictions and experimental progress toward optimizing the amount of simultaneous transverse (spatial) and longitudinal (temporal) intense ion beam current density compression under the appropriate experimental constraints, for applications such as warm dense matter physics, high-energy-density physics, and the heavy ion fusion approach to inertial fusion energy, have been reported. The technique and implementation of plasma-assisted focusing to achieve high levels of intense ion beam compression (beyond the traditional space-charge limit) have been discussed. Encouraging results have been presented from transverse and longitudinal beam focusing experiments on the NTX and NDCX devices, respectively, where both small spot size ($r_b^{foc} < 2$ mm) and short pulse duration ($t_{FWHM} < 5$ ns) have been separately achieved. Fundamental limitations to the experimental realization of optimal longitudinal compression have been well understood through detailed modeling efforts. Simulation predictions and experimental progress of simultaneous transverse and longitudinal compression to a coincident focal plane have been reported. The best results to date using a strong $B_z \sim 80$ kG final-focus solenoid partially filled with high-density plasma are very encouraging, and have resulted in the simultaneous achievement of a spot size $r_b^{foc} \sim 1.5$ mm and pulse duration $t_{FWHM} \sim 2.5$ ns. The U.S. heavy ion fusion program is currently studying the requirements for the upgraded accelerator NDCX-II facility in order to achieve an approximate 50-fold increase in on-target energy density for future warm dense matter experiments.

[1] S. S. Yu, W. R. Meier, R. P. Abbott, J. J. Barnard, T. Brown, D. A. Callahan, C. Debonnel, P. Heitzenroeder, J. F. Latkowski, B. G. Logan, S. J. Pemberton, P. F. Peterson, D. V. Rose, G.-L. Sabbi, W. M. Sharp, and D. R. Welch, Fusion Sci. Technol. **44**, 266 (2003).

[2] A. Ng, T. Ao, F. Perror, M. W. C. Dharma-Wardana, and M. E. Foord, Laser Part. Beams **23**, 527 (2005).

[3] R. P. Drake, *High-Energy-Density Physics* (Springer-Verlag, Berlin, 2006).

[4] B. Y. Sharkov, N. N. Alexeev, M. M. Basko, M. D. Churazov, D. G. Koshkarev, S. A. Medin, Y. N. Orlov, and V. M. Suslin, Nucl. Fusion **45**, S291 (2005).

[5] T. Kikuchi, T. Someya, S. Kawata, M. Nakajima, K. Horioka, and T. Katayama, Nucl. Instrum. Methods Phys. Res. A **558**, 122 (2006).

[6] S. S. Yu, B. G. Logan, J. J. Barnard, F. M. Bieniosek, R. J. Briggs, R. H. Cohen, J. E. Coleman, R. C. Davidson, A. Friedman, E. P. Gilson, L. R. Grisham, D. P. Grote, E. Henestroza, I. D. Kaganovich, M. K. Covo, R. A. Kishek, J. W. Kwan, E. P. Lee, M. A. Leitner, S. M. Lund, A. W. Molvik, C. L. Olson, H. Qin, P. K. Roy, A. B. Sefkow, P. A. Seidl, E. A. Startsev, J. L. Vay, W. L. Waldron, and D. R. Welch, Nucl. Fusion **47**, 721 (2007).

[7] D. A. Callahan, Fusion Eng. Des. **32–33**, 441 (1996).

[8] B. G. Logan and D. A. Callahan, Nucl. Instrum. Methods Phys. Res. A **415**, 468 (1998).

[9] R. B. Miller, *An Introduction to the Physics of Intense Charged Particle Beams* (Plenum, New York, 1982), and references therein (particularly Chap. 4).

[10] R. C. Davidson and H. Qin, *Physics of Intense Charged Partible Beams in High Energy Accelerators* (World Scientific, Singapore, 2001).

[11] D. A. Hammer and N. Rostoker, Phys. Fluids **13**, 1831 (1970).

[12] P. K. Roy, S. S. Yu, S. Eylon, E. Henestroza, A. Anders, F. M. Bieniosek, W. G. Greenway, B. G. Logan, W. L. Waldron, D. L. Vanecek, D. R. Welch, D. V. Rose, R. C. Davidson, P. C. Efthimion, E. P. Gilson, A. B. Sefkow, and W. M. Sharp, Phys. Plasmas **11**, 2890 (2004).

[13] E. Henestroza, S. Eylon, P. K. Roy, S. S. Yu, A. Anders, F. M. Bieniosek, W. G. Greenway, B. G. Logan, R. A. MacGill, D. B. Schuman, D. L. Vanecek, W. L. Waldron, W. M. Sharp, T. L. Houck, R. C. Davidson, P. C. Efthimion, E. P. Gilson, A. B. Sefkow, D. R. Welch, D. V. Rose, and C. L. Olson, Phys. Rev. ST Accel. Beams **7**, 083501 (2004).

[14] P. K. Roy, S. S. Yu, S. Eylon, E. Henestroza, A. Anders, E. P. Gilson, F. M. Bieniosek, W. G. Greenway, B. G. Logan, W. L. Waldron, D. B. Shuman, D. L. Vanecek, D. R. Welch, D. V. Rose, C. Thoma, R. C. Davidson, P. C. Efthimion, I. Kaganovich, A. B. Sefkow, and W. M. Sharp, Nucl. Instrum. Methods Phys. Res. A **544**, 225 (2005).

[15] P. K. Roy, S. S. Yu, E. Henestroza, A. Anders, F. M. Bieniosek, J. Coleman, S. Eylon, W. G. Greenway, M. Leitner, B. G. Logan, W. L. Waldron, D. R. Welch, C. Thoma, A. B. Sefkow, E. Gilson, P. C. Efthimion, and R. C. Davidson, Phys. Rev. Lett. **95**, 234801 (2005).

[16] P. K. Roy, S. S. Yu, W. L. Waldron, A. Anders, D. Baca, J. J. Barnard, F. M. Bieniosek, J. Coleman, R. C. Davidson, P. C. Efthimion, S. Eylon, A. Friedman, E. P. Gilson, W. G. Greenway, E. Henestroza, I. Kaganovich, M. Leitner, B. G. Logan, A. B. Sefkow, P. A. Seidl, W. M. Sharp, C. Thoma, and D. R. Welch, Nucl. Instrum. Methods Phys. Res. A **577**, 223 (2007).

[17] C. K. Birdsall and A. B. Langdon, *Plasma Physics Via Computer Simulation* (McGraw-Hill, New York, 1985).

[18] LSP is a software product developed by ATK Mission Research, Albuquerque, NM 87110, with initial support from the Department of Energy SBIR Program.

[19] F. Winterberg, Plasma Phys. **17**, 69 (1975).

[20] G. Cooperstein, S. A. Goldstein, D. Mosher, R. J. Barker, J. R. Boller, D. G. Colombant, A. Drobot, R. A. Meger, W. F. Oliphant, P. F. Ottinger, F. L. Sandel, S. J. Stephanakis, and F. C. Young, *Laser Interaction and Related Plasma Phenomenona*, edited by J. J. Schwartz, H. Hora, M. Lubin, and B. Yaakobi (Plenum, New York, 1981), Vol. 5, p. 105.

[21] P. F. Ottinger, D. V. Rose, and C. L. Olson, J. Appl. Phys. **75**, 4402 (1994).

[22] A. B. Sefkow and R. C. Davidson, Phys. Rev. ST Accel. Beams **10**, 100101 (2007).

[23] A. B. Sefkow, R. C. Davidson, P. C. Efthimion, E. P. Gilson, I. D. Kaganovich, P. K. Roy, P. A. Seidl, J. E. Coleman, J. J. Barnard, and D. R. Welch, in *Proceedings of the 2007 Particle Accelerator Conference* (IEEE, New York, 2007), p. 2030, http://ieexplore.ieee.org/xpls/abs_all.jsp?arnumber=4441336.

[24] R. C. Davidson and H. Qin, Phys. Rev. ST Accel. Beams **8**, 064201 (2005).

[25] A. B. Sefkow and R. C. Davidson, Phys. Rev. ST Accel. Beams **9**, 090101 (2006).

[26] A. B. Sefkow, R. C. Davidson, P. C. Efthimion, E. P. Gilson, S. S. Yu, P. K. Roy, F. M. Bieniosek, J. E. Coleman, S. Eylon, W. G. Greenway, E. Henestroza, J. W. Kwan, D. L. Vanecek, W. L. Waldron, and D. R. Welch, Phys. Rev. ST Accel. Beams **9**, 052801 (2006).

[27] A. B. Sefkow, R. C. Davidson, I. D. Kaganovich, E. P. Gilson, P. K. Roy, P. A. Seidl, S. S. Yu, D. R. Welch, D. V. Rose, and J. J. Barnard, Nucl. Instrum. Methods Phys. Res. A **577**, 289 (2007).

[28] A. B. Sefkow, R. C. Davidson, and E. P. Gilson, Phys. Rev. ST Accel. Beams **11**, 070101 (2008).

[29] J. E. Coleman, F. M. Bieniosek, E. Henestroza, P. K. Roy, P. A. Seidl, W. L. Waldron, A. B. Sefkow, E. P. Gilson, and D. R. Welch, in *Proceedings of the 2007 Particle Accelerator Conference* (IEEE, New York, 2007), p. 3516, http://www.ieexplore.ieee.org/xpls/abs_all.jsp?arnumber=4440477.

[30] J. Maenchen, L. Wiley, S. Humphries, Jr., E. Peleg, R. N. Sudan, and D. A. Hammer, Phys. Fluids **22**, 555 (1979).

[31] P. F. Ottinger, D. V. Rose, J. M. Neri, and C. L. Olson, J. Appl. Phys. **72**, 395 (1992).

[32] F. F. Chen, *Plasma Physics and Controlled Fusion* (Plenum, New York, 1984).

[33] R. J. Goldston and P. H. Rutherford, *Introduction to Plasma Physics* (Institute of Physics, Bristol, 1995).

[34] P. K. Roy, P. A. Seidl, J. J. Barnard, F. M. Bieniosek, J. E. Coleman, R. C. Davidson, P. Efthimion, E. P. Gilson, J. Y. Jung, M. Leitner, B. G. Logan, D. Ogata, A. Molvik, A. B. Sefkow, W. L. Waldron, and D. R. Welch, in *Proceedings of the 2007 Particle Accelerator Conference* (IEEE, New York, 2007), p. 3519, http://www.ieexplore.ieee.org/xpls/abs_all.jsp?arnumber=4440478.

[35] P. K. Roy, P. A. Seidl, A. Anders, F. M. Bieniosek, J. E. Coleman, E. P. Gilson, W. Greenway, D. P. Grote, J. Y. Jung, M. Leitner, S. M. Lidia, B. G. Logan, A. B. Sefkow, W. L. Waldron, and D. R. Welch, "A space-charge-neutralizing plasma for beam drift compression," Nucl. Instrum. Methods Phys. Res. A (in press).

[36] A. Friedman, J. J. Barnard, R. J. Briggs, R. C. Davidson, M. Dorf, D. P. Grote, E. Henestroza, I. D. Kaganovich, E. P. Lee, M. A. Leitner, B. G. Logan, A. B. Sefkow, W. M. Sharp, W. L. Waldron, D. R. Welch, and S. S. Yu, "Toward a physics design for NDCX-II, a platform for studying ion beam-heated matter," Nucl. Instrum. Methods Phys. Res. A (in press).

[37] W. Sharp, A. Friedman, D. P. Grote, E. Henestroza, M. A. Leitner, and W. L. Waldron, "Developing acceleration schedules for NDCX-II," Nucl. Instrum. Methods Phys. Res. A (in press).